Key Points:
- The WSA-ENLIL + Cone model provides continuous, generally accurate solar wind conditions at Mars
- The WSA-ENLIL + Cone model captures both background and disturbed solar wind conditions accurately
- These continuous solar wind parameters can provide context to planetary and magnetospheric studies

Correspondence to:
R. M. Dewey,
ryan.dewey@colorado.edu

Continuous solar wind forcing knowledge: Providing continuous conditions at Mars with the WSA-ENLIL+Cone model

R. M. Dewey[1,2], D. N. Baker[1], M. L. Mays[3,4], D. A. Brain[1], B. M. Jakosky[1], J. S. Halekas[5], J. E. P. Connerney[4], D. Odstrcil[4,6], J. G. Luhmann[7], and C. O. Lee[7]

[1]Laboratory for Atmospheric and Space Physics, University of Colorado, Boulder, Colorado, USA, [2]Department of Climate and Space Sciences and Engineering, University of Michigan, Ann Arbor, Michigan, USA, [3]Institute for Astrophysics and Computational Sciences, Catholic University of America, Washington, DC, USA, [4]NASA Goddard Space Flight Center, Greenbelt, Maryland, USA, [5]Department of Physics and Astronomy, University of Iowa, Iowa City, Iowa, USA, [6]Computational and Data Sciences, George Mason University, Fairfax, Virginia, USA, [7]Space Sciences Laboratory, University of California, Berkeley, California, USA

Abstract Knowledge of solar wind conditions at Mars is often necessary to study the planet's magnetospheric and ionospheric dynamics. With no continuous upstream solar wind monitor at Mars, studies have used a variety of methods to measure or predict Martian solar wind conditions. In situ measurements, when available, are preferred, but can often be limited in continuity or scope, and so studies have also utilized solar wind proxies, spacecraft flybys, and Earth-Mars alignment to provide solar wind context. Despite the importance of solar wind knowledge and the range of methods used to provide it, the use of solar wind models remains relatively unutilized. This study uses the Wang-Sheeley-Arge (WSA)-ENLIL + Cone solar wind model to calculate solar wind parameters at Mars' orbital location to provide a new approach to determining solar wind conditions at Mars. Comparisons of the model results with observations by the MAVEN spacecraft indicate that the WSA-ENLIL + Cone model can forecast solar wind conditions at Mars as accurately as it has predicted them historically at the Earth, although at Mars the model systematically mispredicts solar wind speed and density, likely a result of magnetogram calibration. Particular focus is placed on modeling the early March 2015 interplanetary coronal mass ejections (ICMEs) that interacted with Mars. Despite the complexity of the ICMEs, the model accurately predicted the speed and arrival time of the ICME-driven interplanetary shock, although it underpredicted other solar wind parameters. These results suggest that solar wind models can be used to provide the necessary general context of the heliospheric conditions to planetary studies.

1. Introduction

Lacking an intrinsic global magnetic field, Mars interacts directly with the solar wind via its upper atmosphere and induced magnetosphere, and as a result, processes in these regions are driven strongly by solar wind conditions [see, e.g., *Brain*, 2006; *Dubinin et al.*, 2011; *Haider et al.*, 2011]. In particular, the solar wind strongly influences ion outflow rates. Solar wind dynamic pressure [e.g., *Lundin et al.*, 2008; *Dubinin et al.*, 2008] and interplanetary magnetic field (IMF) strength [*Nilsson et al.*, 2010] both influence ion outflow rates, and perturbed solar wind conditions associated with increased dynamic pressure, such as corotating interaction regions (CIRs) [e.g., *Edberg et al.*, 2010; *Wei et al.*, 2012] and interplanetary coronal mass ejections (ICMEs) [e.g., *Opgenoorth et al.*, 2013], can dramatically increase these rates. In addition, the solar wind and IMF can also affect Martian magnetospheric boundary locations [e.g., *Brain et al.*, 2005; *Edberg et al.*, 2009b], tail-lobe fields [*Ferguson et al.*, 2005], flux rope dynamics [*Brain et al.*, 2010a; *Briggs et al.*, 2011; *Eastwood et al.*, 2012], and magnetic reconnection [*Eastwood et al.*, 2008; *Halekas et al.*, 2009]. Solar wind interaction with Mars' crustal magnetic fields can also depend on solar wind conditions [see, e.g., *Brain et al.*, 2007, and references therein]. Modeling of the Mars-solar wind interaction corroborates these observational dependencies on the solar wind [e.g., *Ma et al.*, 2004; *Brain et al.*, 2010b; *Najib et al.*, 2011].

Continuous knowledge of solar wind conditions is important for studies at Mars, but there is no continuous upstream solar wind monitor at Mars to supply these measurements. To provide solar wind context to observations, studies have used a variety of techniques. When available, studies use in situ measurements, but these can be limited in instrument (e.g., no magnetometer on Mars Express) or continuity (e.g., orbits that

spend little or no time in the upstream solar wind). When direct measurements are not available, studies have utilized solar wind proxies [e.g., *Crider et al.*, 2003; *Brain et al.*, 2005], spacecraft flybys near Mars [e.g., *Edberg et al.*, 2009a], and/or 1 AU in situ conditions when Earth and Mars share Parker spiral alignment [e.g., *Vennerstrom et al.*, 2003; *Dubinin et al.*, 2009; *Edberg et al.*, 2010; *Opgenoorth et al.*, 2013]. Despite the variety of techniques used to determine upstream solar wind conditions, modeling the solar wind at Mars' orbital location from initial solar conditions has only rarely been used [e.g., *Jakosky et al.*, 2015a].

Several studies have modeled the solar wind at Mars but have focused on model validation of interplanetary shocks instead of providing complete and continuous solar wind conditions. *McKenna-Lawlor et al.* [2008], for instance, examined several solar events in late 2006 to validate the HAFv.2 solar wind model's predictions of interplanetary shocks at several heliospheric locations, including Mars. *Falkenberg et al.* [2011a] utilized multi-point spacecraft observations to constrain simulations of ICME propagation, and *Falkenberg et al.* [2011b] compared the modeled and observed shock events at Mars to improve input parameter methods for solar wind modeling.

Modeling of continuous solar wind conditions throughout the inner heliosphere continues to advance in capability and accuracy [e.g., *Pizzo et al.*, 2011; *Tóth et al.*, 2012; *Lee et al.*, 2013; *Intriligator et al.*, 2015a; *Wu et al.*, 2016a, 2016b] and has been applied to study solar wind-body interactions [e.g., *Baker et al.*, 2013; *Dewey et al.*, 2015]. While many solar wind models exist [e.g., *Hakamada and Akasofu*, 1982; *Tóth et al.*, 2005; *Hayashi*, 2012; *Feng et al.*, 2011, 2012, 2014; *Wu et al.*, 2011; *Yang et al.*, 2011, 2012; *Liou et al.*, 2014; *Intriligator et al.*, 2015b; *Wu et al.*, 2016], here we present upstream solar wind conditions at Mars modeled by the Wang-Sheeley-Arge (WSA)-ENLIL + Cone model over the period from late November 2014 to mid-March 2015. This period corresponds to the beginning of the science mapping phase of the Mars Atmosphere and Volatile Evolution (MAVEN) spacecraft until its last observations of the pristine upstream solar wind for several months due to its orbit. We compare the model results with available upstream MAVEN measurements to determine the validity of this technique of providing continuous upstream solar wind conditions at Mars.

2. Data Sources

2.1. WSA-ENLIL + Cone Model

To model solar wind conditions at Mars' orbital location, we used the WSA-ENLIL + Cone coupled empirical and numerical models installed at the Community Coordinated Modeling Center (CCMC). The WSA (v2.2) model predicts coronal conditions from magnetic synoptic maps of the solar surface and initializes the solar wind flow at 21.5 solar radii based on semiempirical assumptions [see *Wang and Sheeley*, 1992; *Arge and Pizzo*, 2000, and references therein]. Magnetic synoptic maps serve as input to a potential field source surface (PFSS) model that estimates current sheet properties by assuming that the corona is current-free between the photosphere and 2.5 R_S, beyond which the plasma controls the magnetic field, where R_S is the solar radius [*Schatten et al.*, 1969]. At 2.5 R_S, the magnetic field is calculated from a scalar potential that obeys Laplace's equation, and all magnetic field lines are constrained to be open and radial to simulate the effect of the solar wind on the IMF. Between 2.5 R_S and 21.5 R_S, WSA uses the Schatten current sheet model [*Schatten*, 1971] to provide the magnetic topology in the upper corona. The solar wind speed is initialized at the 21.5 R_S boundary based on an empirical formula that relates the solar wind speed and two parameters: (1) the magnetic tube expansion factor, where the expansion factor is calculated by comparing the local field at 21.5 R_S with the associated photospheric field, and (2) the minimum angular separation at the photosphere between an open field footprint and its nearest coronal hole boundary [*Arge et al.*, 2004]. The solar wind density and temperature are determined at the 21.5 R_S boundary by assuming conservation of mass flux and total (thermal and magnetic) pressure balance.

The WSA outer boundary conditions become the inner boundary conditions for the heliospheric model ENLIL. ENLIL (v2.8) is an ideal magnetohydrodynamic, time-dependent, three-dimensional model for which equal temperatures and densities are assumed for electrons and protons and microscopic processes are neglected [*Odstrcil*, 2003]. In Heliocentric Earth Equatorial (HEEQ)-Radial, Tangential, Normal coordinates, ENLIL calculates the tangential IMF component at 21.5 R_S from the radial IMF component and solar wind velocity by assuming Parker spiral geometry. ENLIL scales the inner boundary density and temperature profiles by model free parameters "Dfast" and "Tfast," which correspond to the typical fast stream density (125 cm^{-3})

and temperature (1.5×10^6 K) values, respectively, to provide numerical values at Earth close to measurements and were determined by prior calibration studies. Finally, the ENLIL model uses total variation diminishing algorithms [*Harten*, 1983; see *Tóth and Odstrcil*, 1996] to solve for solar wind velocity, density, temperature, and the IMF throughout the inner heliosphere.

The WSA-ENLIL model predicts background solar wind parameters throughout the computational domain. For this study, a grid spanning 30°–150° in heliospheric colatitude, 0°–360° in longitude, and 0.1 AU to 1.7 AU in radius, with a grid resolution of 4°, was used. For the inner boundary, a sequence of WSA synoptic maps constructed from daily updated magnetograms supplied by the National Solar Observatory's Global Oscillation Network Group (GONG) [*Harvey et al.*, 1996] data set was used. The input map is regridded to a uniform resolution, and the total magnetic flux is calculated, uniformly subtracting any residual monopole moments to ensure a divergence free field [*Lee et al.*, 2013]. The new map is then used as input into the PFSS model in WSA. With 4° angular resolution, the "physical" resolution of corotating physical structures is 7.3 h. Higher grid resolutions can be used in the model to improve numerical resolution, but there are not such high time-resolution corresponding synoptic maps.

The model tends to perform at its best at solar minimum since at active solar times, the solar field can evolve on time scales shorter than the magnetogram cadence so some solar features can be lost at times of high activity [e.g., see *Jian et al.*, 2011, 2015]. Of the modeled solar wind parameters, WSA-ENLIL tends to predict solar wind speed the most reliably [see, e.g., *Gressl et al.*, 2014] and tends to underestimate magnetic field strength and plasma temperature [see *Lee et al.*, 2009; *Jian et al.*, 2015]. Compared to the performance at 1 AU of other coronal and heliospheric models installed at the CCMC, *Jian et al.* [2015] found that WSA-ENLIL used with GONG magnetograms matches the median solar wind density the best and can capture the time series of normalized solar wind parameters well. In contrast, *Jian et al.* [2015] found that the weaknesses of the model at 1 AU include underestimating maximum density, maximum temperature, and maximum IMF strength, and overestimating slow solar wind speed and temperature. *Gressl et al.* [2014] investigated the sensitivity of WSA-ENLIL to different input synoptic maps. While there does not appear to be a trend to any observatory's maps producing systematically better solar wind results, the choice in synoptic map can affect the distributions of solar wind parameters in phase space [*Gressl et al.*, 2014] and can affect the arrival time of individual solar wind features in the simulation [e.g., *Lee et al.*, 2015].

To incorporate CMEs and other transient solar events into the model, we used the WSA-ENLIL + Cone model. In this version of the model, a hydrodynamic structure is inserted into the ENLIL inner boundary from the WSA coronal model using CME parameters derived from coronagraphs. For example, kinematic properties can be derived from the cone model, which assumes radial propagation, constant angular width, and isotropic expansion of a CME to fit a cone shape to white light coronagraph images of the CME to estimate the CME's initial radial speed, size, location, and direction of propagation at 21.5 R_S [*Zhao et al.*, 2002; *Xie et al.*, 2004]. The CME is then inserted into the inner ENLIL boundary (21.5 R_S) as slices of a cloud of homogeneous spherical plasma [*Mays et al.*, 2015]. The cloud (slices) has uniform velocity, density, and temperature, where the initial density and temperature are by default equal to 4 times and 1 time the typical ambient fast-stream mean values, respectively [*Mays et al.*, 2015]. Since ENLIL uses hydrodynamic ejecta and inserts the CME into the inner boundary as a sphere with uniform properties, the model does not simulate ICME magnetic cloud structure but can produce an ICME-driven interplanetary shock by simulating the pileup in front of the CME-like cloud [see *Mays et al.*, 2015]. At the inner boundary, the CME is not initially modeled with an internal magnetic field structure, and as a result, the model can tend to overestimate plasma density and temperature of the propagating structure while underestimate field strength [e.g., *Xie et al.*, 2012]. In this study, CME parameters were determined using the SWPC CME Analysis Tool [*Millward et al.*, 2013]. Since Mars did not interact with any significant ICMEs during the period of study until early March (see below), we incorporated only late February and early March CMEs in the simulation. The cone input parameters for these CMEs are listed in Table 1. While the focus of this study is on the Mars-directed CMEs, we included any additional CMEs during this early March period in case they could influence the propagation of the Mars-directed CMEs. Incorporating CMEs into the model allows WSA-ENLIL + Cone to model total solar wind conditions throughout the inner heliosphere, and statistical studies show the model's validity and accuracy [*Lee et al.*, 2015; *Dewey et al.*, 2015; *Mays et al.*, 2015] (for a discussion of the sensitivity of modeled CMEs to the derived initial parameters, see *Lee et al.* [2013]).

Table 1. Cone Input Parameters at 21.5 R_S for the Early March CMEs

Date	Solar Latitude (°)[a]	Solar Longitude (°)[a]	Cone Radius (°)	Speed (km/s)	xcld[b]	dcld[c]
28-02-2015 T21:48	4	−168	48	1340	1	4
01-03-2015 T12:48	−18	−170	46	900	1	4
03-03-2015 T15:48	−20	−100	42	910	1	4
05-03-2015 T20:36	−20	−95	30	585	1	4
06-03-2015 T04:49	−5	−105	43	900	1	4
06-03-2015 T07:12	−11	−102	47	1450	2	6
07-03-2015 T22:24	−12	−78	45	1200	1	4
10-03-2015 T00:00	−11	−50	32	1200	1	4
10-03-2015 T03:36	6	−45	37	1525	1	4
15-03-2015T02:00	−12	32	45	750	1	4

[a]Positive solar latitude is measured from the solar disk center toward the north rotation axis; positive solar longitude is measured from the solar disk center toward the West limb. The Earth is defined at a solar longitude of 0° (e.g., see Figure 7a).
[b]xcld is the cloud elongation factor in the radial direction (default xcld = 1 is a sphere).
[c]dcld is the cloud density factor (default dcld = 4), the ratio of the injected CME density to the typical fast stream density (Dfast).
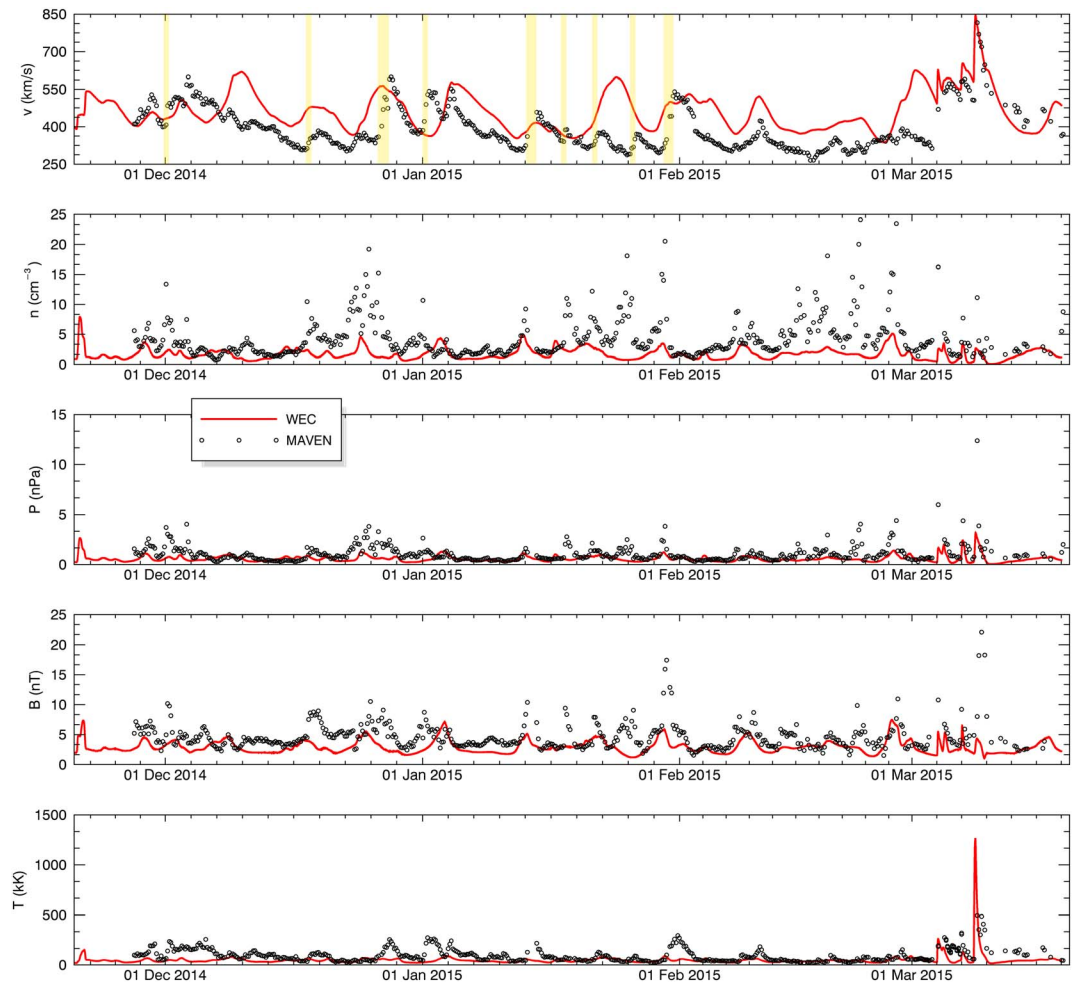
2.2. MAVEN Observations

In conjunction with the model results, we used measurements from several MAVEN spacecraft instruments. In particular, we relied on MAVEN's Solar Wind Ion Analyzer (SWIA) [*Halekas et al.*, 2013] and Magnetometer (MAG) [*Connerney et al.*, 2015a]. There is some uncertainty in the absolute solar wind density measurements from SWIA since the instrument's absolutely sensitivity calibration is uncertain and subject to change. Likewise, temperature measurements derived from SWIA could be overestimated at times since temperature is a partial moment of the solar wind plasma distribution, and for cold distributions, the instrument resolution will artificially broaden the measured distribution. First results from MAG and comparison between the MAG-measured fields and those deduced from electron distributions measured by the Solar Wind Electron Analyzer suggest that MAG is accurately measuring the weak IMF about Mars [*Connerney et al.*, 2015b]. For the purpose of this study, we selected only SWIA and MAG measurements of the "pristine" upstream solar wind (i.e., no exospheric or magnetospheric phenomena present) and averaged these observations over each orbit. In order to determine intervals of the upstream solar wind, we applied several filters to the SWIA and MAG data based on the bulk flow velocity, altitude, sonic Mach number, and the root-mean-square (RMS) magnetic field fluctuations. The criteria are focused on obtaining the most pristine upstream measurements and eliminating false positives for upstream conditions, such as those in the induced magnetosheath and foreshock, so as a result, the filters are conservative in identifying upstream intervals. MAVEN coverage of ICME-driven shock intervals tends to be slightly more sparse than nominal solar wind conditions because the hot shock plasma can fail the Mach number filter.

3. Numerical Modeling and In Situ Parameter Comparisons

We examined the MAVEN data set for signatures of ICMEs and utilized the CCMC *Space Weather Database of Notification*, *Knowledge*, *Information* (kauai.ccmc.gsfc.nasa.gov/DONKI) to search for coronagraph-identified CMEs that could interact with Mars over our period of study. Both methods indicate that Mars did not interact with any ICMEs until the beginning of March 2015. As a result, the sample size of Mars-interacting ICMEs during our period of study is inadequate to analyze ICME conditions at Mars statistically, but allows for a case study of the ICME-driven interplanetary shocks (section 3.3) and a statistical study of the background solar wind over the late November 2014 to mid March 2015 period (section 3.1). Section 3.2 compares the background solar wind performance of the model at Mars with performance at 1 AU.

3.1. Background Solar Wind Statistical Study

Solar wind numerical predictions from the model and observations from the MAVEN spacecraft over the period of study are shown in Figure 1. The panels show radial solar wind speed (*v*), proton density (*n*), dynamic pressure (*P*), IMF strength (*B*), and proton temperature (*T*), respectively. MAVEN data, as discussed above, are orbit averages of solar wind parameters when the spacecraft was measuring the pristine upstream solar wind.

Figure 1. (top to bottom) Comparison between MAVEN solar wind and IMF observations (black circles) with WSA-ENLIL + Cone (WEC) model results (red) over the period of analysis. The MAVEN data are orbit-averaged parameters when the spacecraft was in the pristine upstream solar wind (see text). The values of v, n, P, B, and T are shown in the top to bottom plots, respectively. The highlighted yellow regions in the first panel correspond to corotating interaction regions (CIRs) identified in the MAVEN data set.

As seen in the figure, the ~10 day variations in solar wind parameters are due to solar wind stream structures, e.g., ~22 December to ~01 January and ~01 January to 12 January in the model results. Mars interacts with the background solar wind from ~15 November until ~1 March, and the early March ICMEs thereafter.

Comparing the model results with MAVEN observations, the model appears to capture trends in solar wind parameters well. The correlation coefficients between the model results and MAVEN observations over the 15 November to 1 March period (background solar wind period) are 0.35, 0.29, 0.30, 0.33, and 0.19 for solar wind speed, density, pressure, IMF strength, and temperature, respectively. In addition to capturing the trends in solar wind parameters, the model results also appear to capture the baseline values of P, T, and B well. The model, however, does not always accurately predict the amplitude of deviations from the baseline values, likely a result of the model not incorporating turbulent effects and of the assumed fast- and slow-flow densities [see *Mays et al.*, 2015, and references therein]. In contrast, the model appears to systematically over-predict the solar wind speed by ~70 km/s and, to a lesser degree, underpredict proton density during much of the period of study. These two effects are likely related since solar wind density tends to anticorrelate with solar wind speed in the model, a result of the conservation of momentum flux [see *Lee et al.*, 2013].

Although the model appears to overpredict the baseline solar wind speed at Mars, it appears to capture the velocity transition of solar wind stream interaction regions well. We identified nine CIR signatures that were well recorded in the MAVEN data, which are highlighted yellow regions in Figure 1 (top). CIRs are
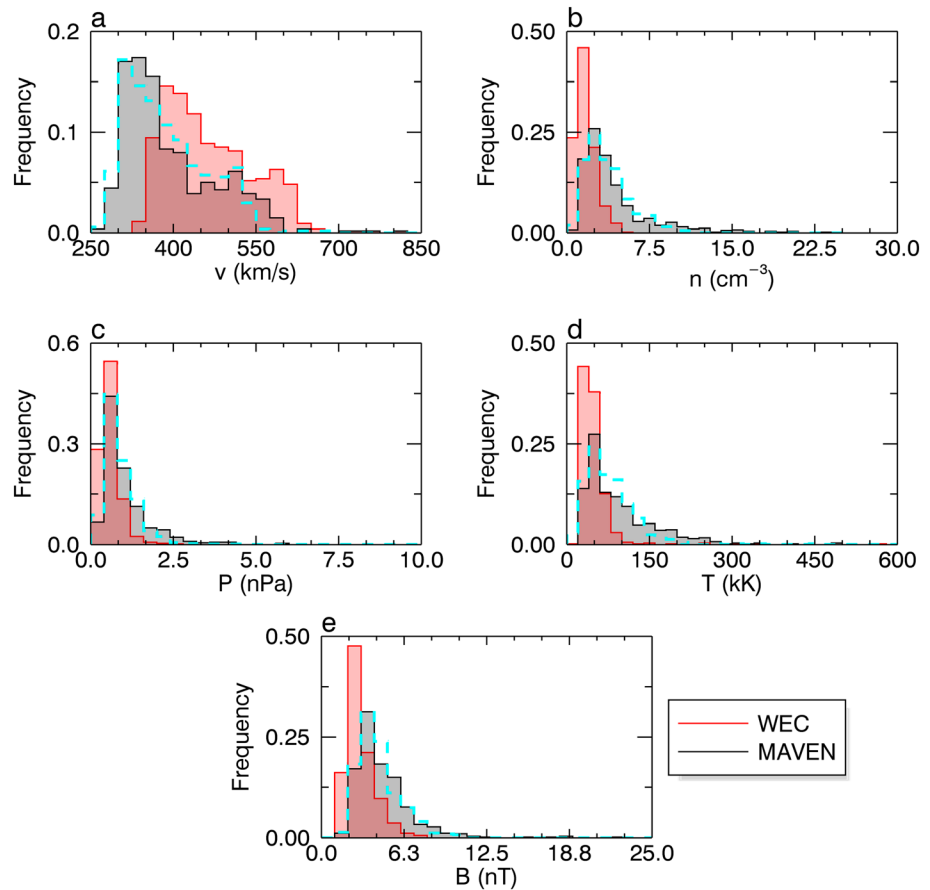
Figure 2. Distributions of the parameters from Figure 1: (a) *v*, (b) *n*, (c) *P*, (d) *T*, and (e) *B*. The model results have been averaged over each MAVEN orbit to match the cadence of the orbit-averaged MAVEN observations. The dashed cyan lines correspond to the respective linearly transformed WSA-ENLIL + Cone (WEC) distribution (see text). The low-frequency, high-value MAVEN bins for each parameters correspond to the early March ICMEs [see *Jakosky et al.*, 2015a].

characterized by a transition from a slow solar wind stream to a fast stream in the time series data, accompanied by increases in density and temperature at the interface between the streams from the interplanetary (IP) shock that forms there. In our analysis, we do not differentiate between the CIR and the shock that forms at the stream interface. The model simulated the first seven CIRs but missed the last two, yielding a probability of detection of ~80%. By comparing the time at the start of the velocity transition as observed by MAVEN and as predicted by the model, the average arrival time error is 13.8 h ± 11.8 h (late) and the average RMS error is 28.6 h ± 5.8 h. These arrival time errors are consistent with previous studies of shock arrival time errors at Mars from ICMEs and interplanetary shocks [*McKenna-Lawlor et al.*, 2008; *Falkenberg et al.*, 2011a; *Falkenberg et al.*, 2011b]. Additionally, by comparing the transition in the velocity profile over each CIR, the model forecasts the velocity increase at 76% ± 14% of the observed value.

Reorganizing the results from Figure 1 as histograms, we see many of the features of the solar wind parameters discussed above more clearly. Figure 2 contains histograms of each of the parameters in Figure 1 as well as histograms of the modeled parameters linearly transformed to match the observed distributions, in cyan. The linear transformations indicate any systematic offsets or scaling in the modeled parameters; a summary of the transforms and their goodness of fit (χ^2) is contained in Table 2 (see below). In Figure 2a, the predicted and measured distributions of solar wind speed match well in profile, but the modeled solar wind speed is systematically higher by 69 km/s as determined by the linear transformation (see Table 2). Likewise, the general shape of the proton density distributions matches well although the modeled distribution is compressed by a factor of 2.25. The compression of the modeled n distribution and the systematic overestimation in the v distribution largely explain the linear transformation of the P distribution ($P = nmv^2$, where m is the proton mass). Although the modeled solar wind pressure distribution is compressed in

Table 2. Summary of Model Parameter Linear Transformations

| Parameter | Linear Transformation[a] | | χ^2 |
	Scaling	Offset	
v	1.00	-69 km/s	1.67
n	2.25	0.0 cm^{-3}	1.05
P	1.83	-0.13 nPa	0.40
T	3.00	-48 kK	2.77
B	1.47	0.0 nT	0.89

[a]Linear transformations are given by $scaling \times parameter + offset$.

comparison to MAVEN observations, we see close agreement between the baseline (distribution peak) pressure of ~1 nPa. In Figure 2d, we see good agreement between the baseline solar wind temperature of ~50 kK, but the modeled distribution underestimates T by a factor of about 3. IMF strength is likewise underestimated, but only by a factor of 1.47 and requiring no systematic offset.

Comparing the entire distributions for each parameter, the ratio of the median values modeled by WSA-ENLIL + Cone and observed by MAVEN (i.e., v_{model}/v_{MAVEN}) over the 15 November to 1 March period is 1.20 for solar wind speed, 0.49 for proton density, 0.65 for dynamic pressure, 0.57 for proton temperature, and 0.69 for IMF strength. Likewise, the mean square errors (MSEs) between the model results and observations over the background solar wind period are 1.06×10^4 km^2/s^2, 18.1 cm^{-6}, 0.60 nPa^2, 4.85×10^3 kK^2, and 6.04 nT^2, respectively. These statistics are summarized in Table 3 and do not include the linear transformations.

To determine the uniqueness of the linear transformations, we examined χ^2 in the parameter space about each transformation, as shown in Figure 3. We also used Kolmogorov-Smirnov (K-S) testing to determine a region of parameter space, in which the linearly transformed parameter distribution matched the observed distribution above the 95% confidence level. The smallest χ^2 within the K-S valid region provides the most robust transformation. As expected, the K-S region tends to enclose the smallest χ^2 of the entire parameter space, as seen in Figures 3a, 3c, and 3e for v, P, and B, respectively. The region of best fit for v is more constrained than for other parameters (e.g., n, P, and B) and forms a narrow line in parameter space, suggesting that a small offset for v has the same effect as a small change in scaling. Although the χ^2 for v is the second largest of the transformations (see Table 2), the narrow valid region in parameter space indicates a unique transformation for v. In contrast, the region of best fit for n has a large spread in parameter space and the K-S region encloses the largest area of all parameters, suggesting that the transformation for n is not as well constrained. The K-S region for n encloses an offset of ±0; transforming n requires only a scaling factor. Similar to n, the fit for P in Figure 3c also shows considerable spread, although the transformed P matches the MAVEN distribution the best with the smallest χ^2 of 0.40. The K-S regions for P and T enclose neither an offset of ±0 nor a scaling of 1, requiring both an expansion factor and systematic offset for their respective linear transformations. At a scaling factor of 3.0 and offset of -48 kK, the transformation for T is the most significant

Table 3. Summary of Model Performance Statistics at Mars and Earth

Parameter		Correlation Coefficient	Median Ratio	Mean Square Error
v	Mars[a]	0.35	1.20	1.06×10^4 km^2/s^2
	Earth[a]		1.14	
	Jian et al.[b]	0.50	1.15	1.22×10^4 km^2/s^2
n	Mars	0.29	0.49	18.1 cm^{-6}
	Earth		0.76	
	Jian et al.	0.22	1.07	24 cm^{-6}
P	Mars	0.30	0.65	0.60 nPa^2
	Earth		0.97	
	Jian et al.			
B	Mars	0.33	0.69	6.04 nT^2
	Earth		0.71	
	Jian et al.	0.20	0.19	17 nT^2
T	Mars	0.19	0.57	4.85×10^3 kK^2
	Earth		0.82	
	Jian et al.	0.30	0.56	7.5×10^3 kK^2

[a]Comparisons over the period 15 November to 1 March 2015.
[b]Approximate values from Jian et al. [2015] for the WSA-ENLIL model with GONG magnetograms.
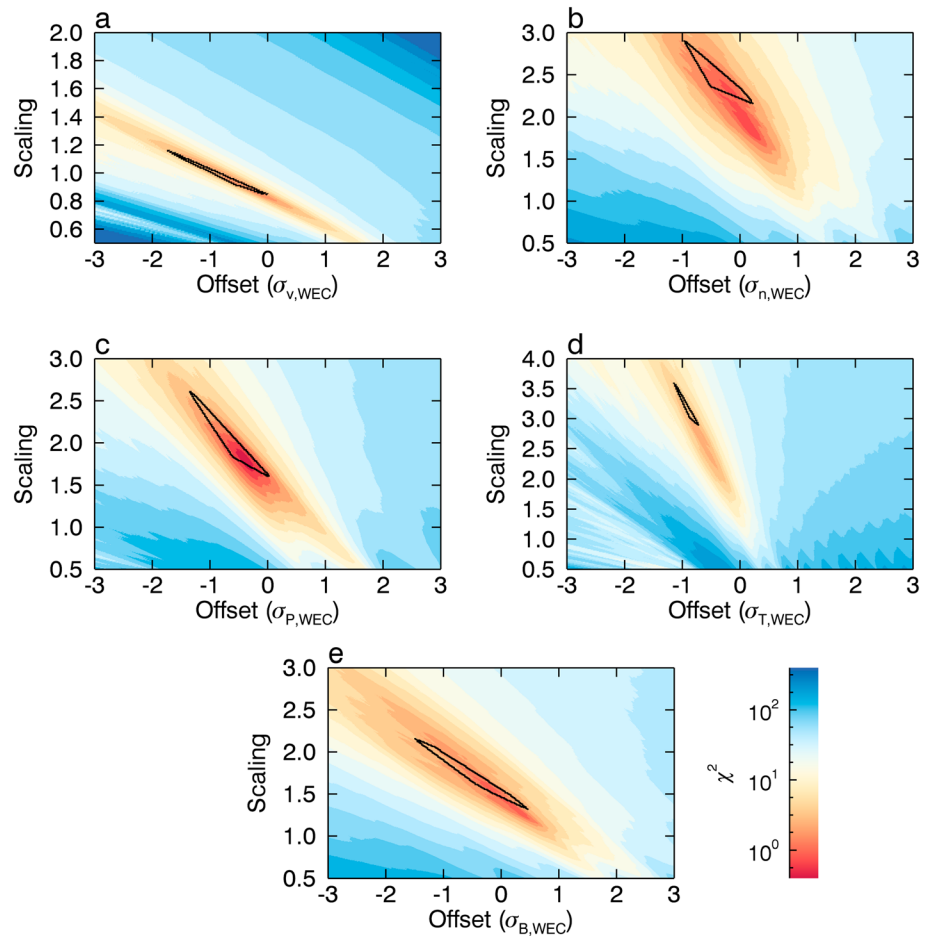
Figure 3. Parameter space for the linear transformations in Figure 2: (a) v, (b) n, (c) P, (d) T, and (e) B transforms. The colors correspond to the χ^2 value as indicted by the color bar; all plots share the same color bar scaling. The black polygons and the area they enclose indicate the region of parameter space that satisfy K-S testing at the 95% confidence level. Note that Figures 3b, 3c, and 3e show similar regions of parameter space, while Figure 3a has been zoomed in and Figure 3d has been zoomed out.

and has largest χ^2. The large transformation required for T is not unexpected, however, as the model can underestimate T by up to an order of magnitude [see *Jian et al.*, 2011], a recognized limitation of the model. Finally, the K-S region for B forms a line in parameter space, although less constrained than for v. Similar to the transformation for n, the K-S region for B encloses an offset of ±0.

To complete the parameter comparisons, Figure 4 contains histograms of the IMF elevation angle (the angle between the IMF direction and the orbital plane) and the IMF spiral angle (the angle of rotation of the IMF in the orbital plane). MAVEN observed a broad, symmetric elevation angle distribution centered at zero degrees (IMF confined to the orbital plane). The model matches the general peak and symmetry of the distribution, although the angles in the tail of the distribution are sparsely populated. The spiral angle follows a similar trend. MAVEN observed a binomial distribution with peaks at 115° and 295°, consistent with a Parker spiral angle of ~65°. The model, in contrast, predicted a binomial distribution with peaks at 135° and 315°, corresponding to a Parker spiral angle of ~45°, with a depletion of intermediate angles compared to the observed distribution. The model's underprediction of the Parker spiral angle over the period of study is consistent with its systematic overprediction of the solar wind velocity, as described above.

Although the model tends to underestimate the Parker spiral angle, the model captures IMF sectors well. The cumulative frequency of the IMF spiral angle between 90° and 270° (IMF "away" sector) agrees well between the two distributions. MAVEN observed a spiral angle in this range with a frequency of 0.485, and the model predicted it with a frequency of 0.442. Contingency analysis of the IMF sector indicates that the model
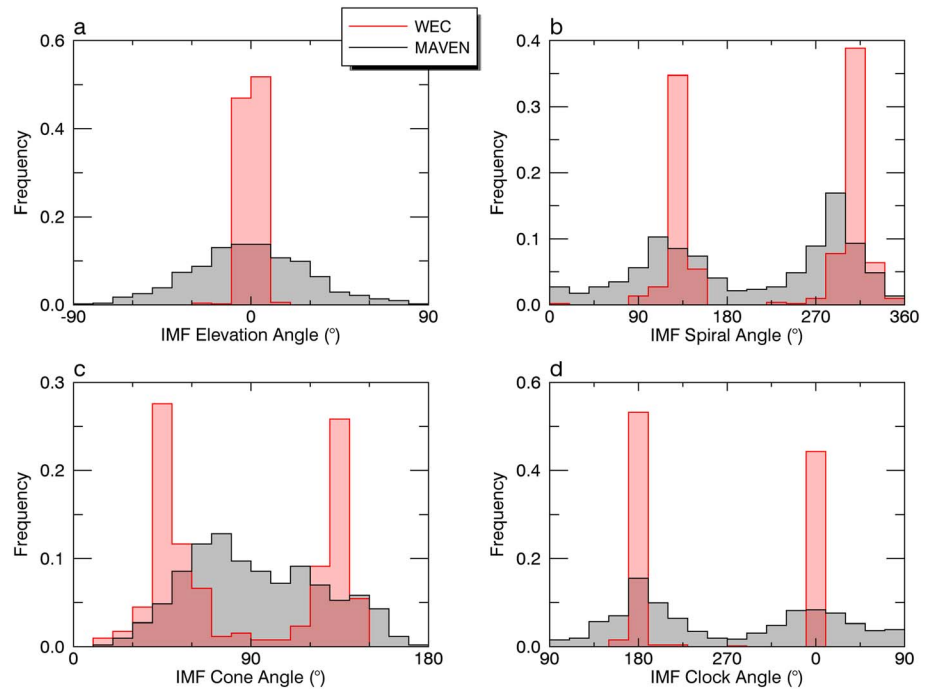
Figure 4. Distributions of the IMF (a) elevation, (b) spiral, (c) cone, and (d) clock angles in the same format as Figure 2. Spiral angles of 0°, 90°, 180°, or 270° indicate that the component of the IMF in Mars' orbital plane points planetward, dawnward, sunward, or duskward, respectively. Clock angles of 0°, 90°, 180°, or 270° indicate that the component of the IMF perpendicular to the Sun-Mars line points dawnward, northward, duskward, or southward, respectively. The elevation and spiral angles form a complete set of angles, as do the cone and clock angles.

accurately predicted the IMF sector, either away ($B_r > 0$) or "toward" ($B_r < 0$), where B_r is the radial component of the IMF, correctly on 74.6% of the MAVEN orbits. The model predicted correctly the away sector on 181 orbits and the toward sector on 203 orbits, and it predicted incorrectly the away sector on 84 orbits (i.e., the model predicted the toward sector) and the toward sector on 47 orbits. The model's performance thus produces a Heidke Skill Score of 0.493 in accurately predicting the IMF sector. These results appear to be similar to the model's capabilities at Earth [*Jian et al.*, 2011].

For comparison with the model's performance at Mercury (see Figure 6 from *Dewey et al.* [2015, middle row]), Figure 4 also includes distributions of the IMF clock angle (the angle of rotation of the IMF around the Sun-Mars line) and cone angle (the angle between the IMF direction and the Sun-Mars line). MAVEN observed a symmetric, bimodal distribution of clock angles most heavily populated at low dawn and dusk angles. The model matches the bimodality but does not match the intermediate angles, similar to the model's results at Mercury. The cone angle follows a different trend. MAVEN observed a nearly symmetric cone angle distribution about 90° (magnetic field perpendicular to the Sun-Mars line). The model, in contrast, predicted a bimodal distribution with peaks at ~45° and ~135° and with a depletion of angles around 90°. Although the modeled cone angle distribution at Mars matches the modeled distribution at Mercury, the observed distributions show significant difference. MESSENGER observed a bimodal distribution with a skew toward larger cone angles at Mercury compared to MAVEN's observations of a symmetric, broad distribution. The differences between the observed cone angle distributions are likely associated with the time averaging between the two distributions, the total number of observations, and the increased heliospheric distance of Mars. A common feature of all four IMF angle comparisons is that the model underestimates the frequency of non-Parker spiral angles, which is due to ENLIL not treating turbulent or microscopic fluctuations.

3.2. Comparison With 1 AU Studies

To provide additional context to the model results at Mars, we compare the background solar wind statistical study above to similar studies at 1 AU. During the period of study, the Earth interacted with several minor ICMEs, so the conditions at Earth (not shown here) do not represent the background solar wind as well as

the pre-March conditions at Mars. Since outlying values, such as those from ICME events, can influence correlation coefficient and MSE statistics strongly, we report only the median ratio statistics at 1 AU over the 15 November to 1 March period in Table 3 to keep with the background solar wind comparison with Mars. Table 3 also lists statistics from *Jian et al.* [2015] to provide additional context to the Martian results. *Jian et al.* [2015] compared various solar wind models with in situ observations at 1 AU over seven Carrington rotations (~191 days) in 2007, chosen because of the low solar activity during this time. Although *Jian et al.* [2015] compared several models, in keeping with the above methods, only the statistics from the WSA-ENLIL model with GONG magnetograms are listed in Table 3.

Overall, comparing the background solar wind statistics at Mars to those at 1 AU, the model appears to capture trends as accurately at Mars' location that at 1 AU on average, although the model tends to mispredict *v* and *n* more strongly at Mars. The correlation coefficients for solar wind speed and temperature are smaller at Mars than those found by *Jian et al.*, while the *n* and *B* coefficients are improved at Mars over correlations at 1 AU. The MSEs at Mars are all smaller than those for the 2007 background solar wind conditions at Earth. The most significant MSE difference between Mars and 1 AU is IMF strength. Finally, comparing the median ratios at Mars and 1 AU, the model underpredicts *n* at both Mars at Earth during the period of study but predicts *B* more accurately at both locations compared with 2007 results. The median *v*, *n*, *P*, and *T* are each mispredicted more strongly at Mars than at Earth over the period of study, although the *T* median ratio at Mars is similar to that found for 2007. The most significant median ratio difference between Earth and Mars over the period of study is the proton density; the median *n* ratio dropped from 0.76 to 0.47, which has a strong bearing on the calculated dynamic pressure, which drops from 0.97 to 0.65. Several factors contribute to these statistics: correlation coefficients depend on both the timing of solar wind features and the relative change of solar wind parameters between the model and observations; median ratios depend only on systematic offsets or scaling; and MSEs depend on both the timing of features and systematic offsets/scaling. Taken together, the correlations and parameter distributions indicate that solar wind modeling at Mars over our period of study captures solar wind trends and features well.

3.3. 8 March ICME Case Study

In addition to capturing the quiescent background solar wind conditions, the WSA-ENLIL + Cone model must also accurately predict disturbed conditions if it is to be used to provide solar wind context at Mars. Since there are too few ICMEs during our period of study for a significant statistical study, we compare the model results with observations of the 8 March ICME, the most significant ICME during our period of study [*Jakosky et al.*, 2015a], to assess the performance of the model in predicting disturbed conditions. Model results and MAVEN observations of the disturbed solar wind conditions of early March 2015 at Mars are shown in Figure 5. Aside from the mispredicted fast stream at the beginning of the period, the model appears to accurately reflect the general background solar wind conditions and solar wind trends over this period, particularly for solar wind speed.

As discussed by *Jakosky et al.* [2015a], the 8 March ICME that impacted Mars was composed of two individual transients that merged en route to the planet. From coronagraph images as shown in Figure 6, the two CMEs erupted in close succession on 6 March (04:49 UT and 07:12 UT) from just beyond the solar limb and traveling in the direction of 105°E ± 10° longitude (HEEQ coordinates). The first CME had a flux-rope morphology with a bright core, as seen in Figure 6a, and the leading edge of the CME had a speed of about ~900 ± 100 km/s with a nearly equatorial latitude. The trailing edge of the first CME interacted with and was overtaken by the faster, southern part of the second CME as seen in Figures 6b–6d, which had a speed of ~1450 ± 150 km/s and latitude of −10°. The slower, equatorial portion of the second CME may have been retarded by the previous CME, with a speed of ~800 ± 150 km/s. Due to observations of extended eruptions and bright CME features, a cloud elongation factor of 2 (default of 1) and cloud density ratio of 6 (default of 4) were used for the second, faster CME in the model. Both 6 March CMEs were included in the WSA-ENLIL + Cone modeling with inner boundary input speeds of 900 km/s and 1500 km/s, respectively, which predicted the interplanetary (IP) shock of the merged ICME to arrive at Mars ~11:40 UT on 8 March.

MAVEN observations, however, indicate that the merged ICME IP shock structure arrived at ~15:22 UT on 8 March. Upstream-averaged MAVEN observations of the ICME-driven shock revealed a solar wind speed of 816 km/s, density of 11.1 cm^{-3}, pressure of 12.4 nPa, and IMF strength of 8.0 nT. While the model captured the arrival time and peak speed (845 km/s) of the ICME-driven shock well, it underestimated the peak density
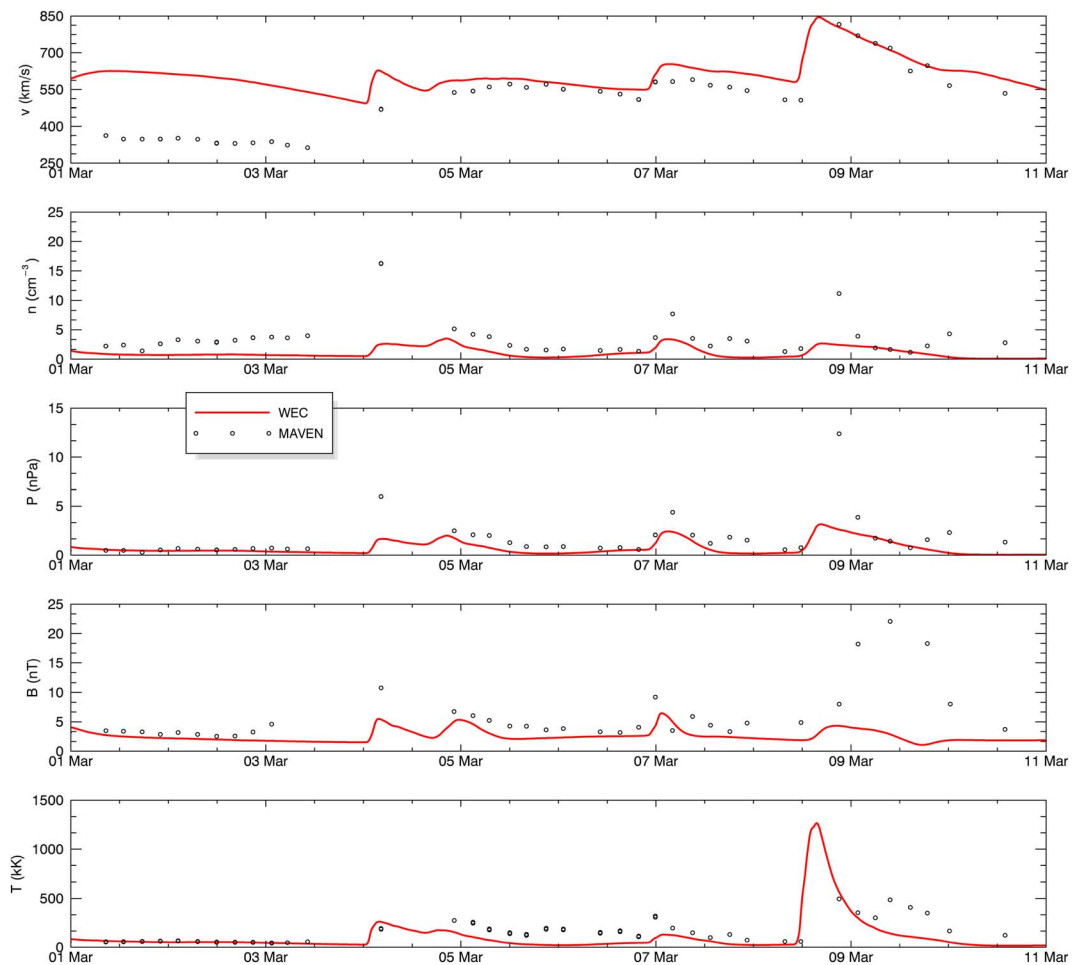
Figure 5. Solar wind parameter comparison at Mars during early March 2015 in the same format as Figure 1.

($1.8\,cm^{-3}$), pressure ($5.4\,nPa$), and IMF strength ($3.0\,nT$). The absolute error in shock arrival time ($3.7\,h$) is significantly less than the average absolute error ($19.2\,h \pm 4.7\,h$) found by *Falkenberg et al.* [2011b] at Mars, and the n, P, and B mispredictions are recognized challenges of the model [e.g., *Xie et al.*, 2012; *Lee et al.*, 2015; *Dewey et al.*, 2015; *Jian et al.*, 2015].

4. Discussion and Conclusions

In this paper we expanded on previous techniques of determining solar wind conditions at Mars by modeling solar wind conditions from the solar surface to Mars' orbital location using the WSA-ENLIL + Cone model. We compared the modeling results with in situ solar wind and IMF measurements from the MAVEN spacecraft over the period from late November 2014 to mid March 2015. Initial modeling and spacecraft observations indicate that Mars interacted mostly with the background solar wind until the beginning of March when a series of ICMEs interacted with the planet. The relatively quiet solar wind conditions during the period of study allowed us to perform a background solar wind statistical study and ICME case study of the model's performance at Mars.

Our comparisons between the model results and in situ data show generally good agreement for both solar wind and IMF parameters, but the model results show significant systematic offsets in both solar wind speed and proton density. The model systematically overpredicts solar wind speed by $69\,km/s$ and underpredicts proton density by a factor of 2.25, which have a significant bearing on the calculated solar wind dynamic pressure. Since the model applies conservation of momentum flux in initializing solar wind conditions, the mispredictions of solar wind speed and proton density are likely connected. The model also underpredicts
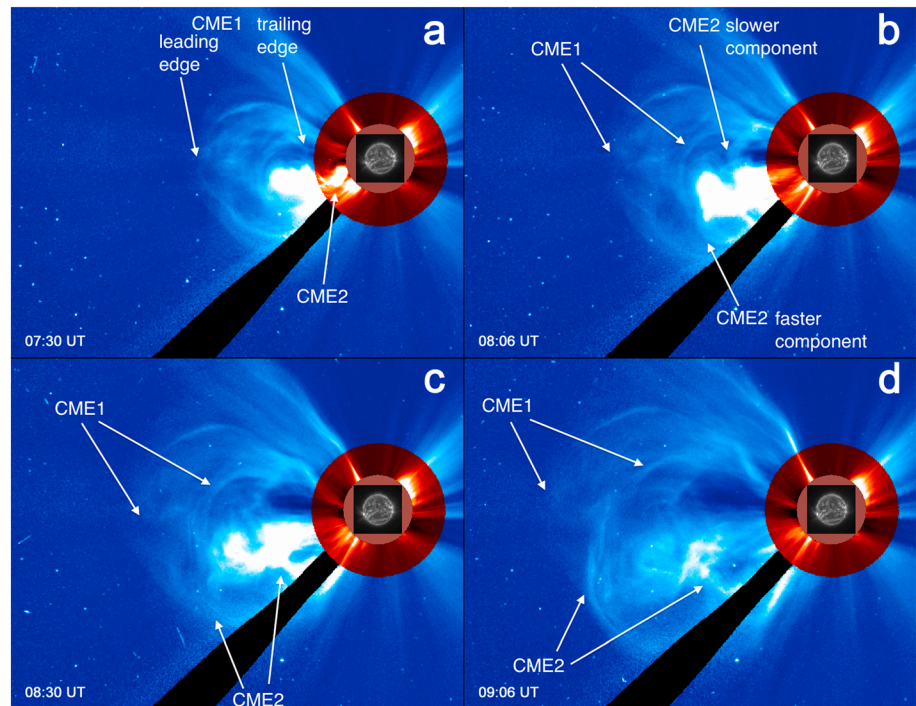
Figure 6. Composite coronagraph images of the eruptions of the 6 March CMEs provided by helioviewer.org. The time of each SOHO/Large Angle and Spectrometric Coronagraph C3 observation (blue coronagraph) is listed in the lower left of each panel. See text for details.

IMF strength by a factor of 1.5. Solar wind temperature requires the most significant transformation—scaling by a factor of 3.0 and an offset of −48 kK—although these mispredictions are a recognized limitation of the model. Meanwhile, if any systematic offsets in the temperature moments at either Mars or 1 AU exist, they will most likely involve an overestimation of the temperature, since finite instrumental angular and energy resolution will always broaden the measured distribution, an effect that is difficult to correct for without model-dependent and computationally expensive deconvolution. Such an effect, if present, could also potentially contribute to the disagreement between model and measured temperatures both at 1 AU and at Mars. We examined the parameter space about these linear transformations to determine their uniqueness and found the best fit with solar wind dynamic pressure and IMF strength, although the systematic offset in solar wind velocity was the most constrained in parameter space. Unique or well-constrained transformations allow for better practical use of the model results and can help identify limitations of the model.

Several factors could also contribute to these mispredictions. During the period of study, as seen in Figure 7a, Mars remained ~120°E of the Earth in the ecliptic plane so the magnetograms collected at Earth to serve as input into WSA-ENLIL were ~2 weeks "old" when conditions are propagated to Mars. The mispredictions, however, may be more intrinsic to the model, or more likely, to the calibration of the magnetograms, since they begin to appear during MAVEN's cruise to Mars. Figures 7b and 7c shows the continuous solar wind speed measurements from SWIA and ACE, respectively, and the model results at both spacecraft during a portion of MAVEN's cruise from mid-March 2014 to mid-July 2014. The systematic velocity offsets begin to appear in the model results at both spacecraft locations around early May when MAVEN was still near the Earth's ecliptic longitude (~13°E of Earth). The appearance of the offset at both locations, the fact that earlier studies of the model do not show these systematic velocity trends [see, e.g., *Jian et al.*, 2015], and the well-constrained nature of the offset in parameter space suggest that the mispredictions are likely connected to magnetogram calibration issues and/or that the WSA model assumptions may not be as valid for this period.

Despite the systematic trends in the solar wind parameter distributions, the model captures corotating interaction regions and IMF sectors well. The model simulated seven of the nine CIRs identified at Mars during the
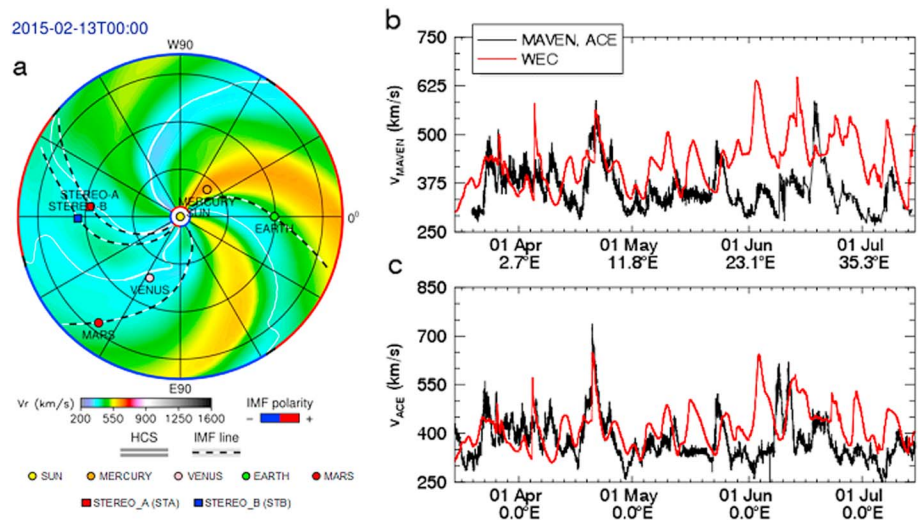
Figure 7. (a) Modeled radial solar wind speed, viewed from the north ecliptic pole, in the ecliptic plane from the WSA-ENLIL + Cone (WEC) model for 13 February 2015. The scale for v_r is given by the color bar. The locations of spacecraft, planets, and the Sun are indicated by small symbols. Other features are listed in the legend, including crossings of the heliospheric current sheet in the ecliptic plane. There were no CMEs observed during this time. (b) SWIA solar wind speed measurements (black) and model results (red) during a portion of MAVEN's cruise phase from mid-March to mid-July 2014. The horizontal axis ticks include the date and MAVEN's ecliptic longitude, as defined in Figure 7a, at several points during the cruise. (c) ACE solar wind speed observations (black) and model results at ACE (red) over the MAVEN cruise period shown in Figure 7b. Earth is taken to be fixed at an ecliptic longitude of 0°E as in Figure 7a.

period of study, and it predicted the arrival time of them $13.8\,h \pm 11.8\,h$ late on average and predicted the velocity transition across the CIR at 76% the observed value on average. For IMF sector, the model accurately predicted the sector on 74.6% of MAVEN's orbits with a Heidke Skill Score of 0.493. Since the best fit IMF strength linear transformation only involves a scaling term and not an offset term, the model's IMF sector prediction would not be affected the systematic trends in the modeled IMF parameter distribution. IMF angle analysis indicates, however, that the model nominally predicts the IMF confined near the orbital plane and at a Parker spiral angle, the latter of which would be affected by solar wind speed mispredictions. The correction of the systematic velocity trends in the model results may improve IMF angle comparisons and sector prediction.

In addition to comparing model results with MAVEN observations, we utilized comparisons at 1 AU to provide additional context to the model's background solar wind performance at Mars' orbital location. Comparisons between the model's performance at Mars and both its performance at Earth during the period of study and in *Jian et al.* [2015] indicate that the model captured solar wind trends at Mars' orbital location over the background solar wind period as accurately as at 1 AU on average and suggest that from a statistical basis, the model generally produces accurate conditions at Mars' orbital location, although the mispredictions at Mars were more extensive than that at 1 AU. One influence on the statistical comparisons between Mars and Earth is the planets' heliocentric locations during the study. Given the locations of Mars and Earth in the heliosphere (see Figure 7a), Earth encountered solar wind streams ~20 days before Mars. Since our statistical comparisons cover the same range of dates at both locations (15 November to 1 March), the solar wind features compared between the model and observations were different at Earth than at Mars. For example, the first ~20 days of the Mars time series in Figure 1 corresponds to the ~20 days before our period of study for Earth. Nevertheless, correcting the systematic mispredictions in the modeling of the solar wind speed and proton density using WSA-ENLIL would further improve the accuracy and validity of the modeled solar wind conditions at Mars.

To accompany the statistical study of the background solar wind, we examined the 8 March ICME [*Jakosky et al.*, 2015a] as a case study for the model's performance in predicting disturbed solar wind conditions. Despite the complexity of the ICME as several merged CMEs and the challenge that poses to modeling, the model simulated the arrival time and speed of the ICME-driven shock well, although it underpredicted

other solar wind parameters, which has been seen in other studies [e.g., *Xie et al.*, 2012; *Lee et al.*, 2015; *Dewey et al.*, 2015]. While only a case study, the model's performance indicates that it can capture disturbed conditions well in addition to the background solar wind.

To investigate further the source of the systematic trends in the solar wind parameters, future work should focus on the sensitivity of modeling at Mars to input magnetograms and magnetogram calibrations and can compare modeling results using different input observatories (e.g., GONG, Air Force Data Assimilative Photospheric Flux Transport model [*Arge et al.*, 2010], and National Solar Observatory). Furthermore, June through August 2016 provide the additional benefit of favorable alignment between Mars and Earth, beginning with radial alignment and then Parker spiral geometry, allowing solar wind conditions and results at Mars to be directly compared with those at Earth. Studies performed over the next few years could also benefit from the upcoming solar minimum, during which the model may predict the solar wind more accurately since daily updated synoptic maps can better capture the slower evolution of solar conditions at solar minimum compared to the more rapidly evolving conditions at solar maximum. Finally, a future investigation would benefit from a longer period of study and with more solar activity, allowing the model to be validated over a greater range of conditions and to allow for statistical analysis of disturbed solar wind conditions modeled at Mars. With the approaching solar minimum, validating the model with more solar activity may not be possible for the next several years.

We conclude that solar wind modeling tools can be used to provide solar wind context at Mars' orbital location for planetary studies. Although this study focused on the WSA-ENLIL + Cone model, other solar wind models [e.g., *Hakamada and Akasofu*, 1982; *Tóth et al.*, 2005; *Hayashi*, 2012; *Feng et al.*, 2011, 2012, 2014; *Wu et al.*, 2011; *Yang et al.*, 2011, 2012; *Liou et al.*, 2014; *Intriligator et al.*, 2015b; *Wu et al.*, 2016] could also be utilized to provide continuous upstream conditions at Mars. A particular advantage of the continuous conditions provided by models is that they can be used to fill any data gaps in in situ observations. With MAVEN specifically, the spacecraft's deep-dip campaigns and evolving orbit will prevent it from sampling upstream solar wind conditions from days to months at a time [*Jakosky et al.*, 2015b], allowing solar wind models to fill these coverage gaps and supplement Mars Express observations, especially IMF observations. More generally, however, this technique can be used in conjunction with other techniques of determining solar wind conditions at Mars, such as solar wind proxies and Parker spiral alignments with the Earth, to provide the most thorough and global context to Martian studies.

References

Arge, C. N., and V. J. Pizzo (2000), Improvement in the prediction of SW conditions using near-real-time solar magnetic field updates, *J. Geophys. Res.*, *105*, 10,465–10,479, doi:10.1029/1999JA000262.

Arge, C. N., J. G. Luhmann, D. Odstrcil, C. J. Schrijver, and Y. Li (2004), Stream structure and coronal sources of the solar wind during the May 12th, 1997 CME, *J. Atmos. Sol. Terr. Phys.*, *66*, 1295–1309.

Arge, C. N., Henney, C. J., Koller, J., Compeau, C. R., Young, S., MacKenzie, D., Fay, A., and Harvey, J. W. (2010), Air Force Data Assimilative Photospheric Flux Transport (ADAPT) model, in *AIP Conf. Proc.*, vol. 1216, pp. 343–346, Am. Inst. of Phys., Melville, New York, doi:10.1063/1.3395870.

Baker, D. N., et al. (2013), Solar wind forcing at Mercury: WSA-ENLIL model results, *J. Geophys. Res. Space Physics*, *118*, 45–57, doi:10.1029/2012JA018064.

Brain, D. A. (2006), Mars Global Surveyor measurements of the Martian solar wind interaction, *Space Sci. Rev.*, *126*, 77–112, doi:10.1007/s11214-006-9122-x.

Brain, D. A., J. S. Halekas, R. J. Lillis, D. L. Mitchell, R. P. Lin, and D. H. Crider (2005), Variability of the altitude of the Martian sheath, *Geophys. Res. Lett.*, *32*, L18203, doi:10.1029/2005GL023126.

Brain, D. A., R. J. Lillis, D. L. Mitchell, J. S. Halekas, and R. P. Lin (2007), Electron pitch angle distributions as indicators of magnetic field topology near Mars, *J. Geophys. Res.*, *112*, A09201, doi:10.1029/2007JA012435.

Brain, D. A., A. H. Baker, J. Briggs, J. P. Eastwood, J. S. Halekas, and T.-D. Phan (2010a), Episodic detachment of Martian crustal magnetic fields leading to bulk atmospheric plasma escape, *Geophys. Res. Lett.*, *37*, L14108, doi:10.1029/2010GL043916.

Brain, D., et al. (2010b), A comparison of global models for the solar wind interaction with Mars, *Icarus*, *206*, 149–151, doi:10.1016/j.icarus.2009.06.030.

Briggs, J. A., D. A. Brain, M. L. Cartwright, J. P. Eastwood, and J. S. Halekas (2011), A statistical study of flux ropes in the Martian magnetosphere, *Planet. Space Sci.*, *59*, 1498–1505, doi:10.1016/j.pss.2011.06.010.

Connerney, J. E. P., J. Espley, P. Lawton, S. Murphy, J. Odom, R. Oliverson, and D. Sheppard (2015a), The MAVEN magnetic field investigation, *Space Sci. Rev.*, *169*, doi:10.1007/s11214-015-0169-4.

Connerney, J. E. P., J. R. Espley, G. A. DiBraccio, J. R. Gruesbeck, R. J. Oliversen, D. L. Mitchell, J. Haleskas, C. Mazelle, D. Brain, and B. M. Jakosky (2015b), First results of the MAVEN magnetic field investigation, *Geophys. Res. Lett.*, *42*, 8819–8827, doi:10.1002/2015GL065366.

Crider, D. H., D. Vignes, A. M. Krymskii, T. K. Breus, N. F. Ness, D. L. Mitchell, J. A. Slavin, and M. H. Acuña (2003), A proxy for determining solar wind dynamic pressure at Mars using Mars Global Surveyor data, *J. Geophys. Res.*, *108*(A12), 1461, doi:10.1029/2003JA009875.

Dewey, R. M., et al. (2015), Improving solar wind modeling at Mercury: Incorporating transient solar phenomena into the WSA-ENLIL model with the Cone extension, *J. Geophys. Res. Space Physics*, *120*, 5667–5685, doi:10.1002/2015JA021194.

Dubinin, E., et al. (2008), Structure and dynamics of the solar wind/ ionosphere interface on Mars: MEX-ASPERA-3 and MEX-MARSIS observations, *Geophys. Res. Lett.*, *35*, L11103, doi:10.1029/2008GL033730.

Dubinin, E., M. Fränz, J. Woch, F. Duru, D. Gurnett, R. Modolo, S. Barabash, and R. Lundin (2009), Ionospheric storms on Mars: Impact of the corotating interaction region, *Geophys. Res. Lett.*, *360*, L01105, doi:10.1029/2008GL036559.

Dubinin, E., M. Fränz, A. Fedorov, R. Lundin, N. Edberg, F. Duru, and O. Vaisberg (2011), Ion energization and escape on Mars and Venus, *Space Sci. Rev.*, *162*, 173–211, doi:10.1007/s11214-011-9831-7.

Eastwood, J. P., D. A. Brain, J. S. Halekas, J. F. Drake, T. D. Phan, M. Øieroset, D. L. Mitchell, R. P. Lin, and M. Acuña (2008), Evidence for collisionless magnetic reconnection at Mars, *Geophys. Res. Lett.*, *35*, L02106, doi:10.1029/2007GL032289.

Eastwood, J. P., J. J. H. Videira, D. A. Brain, and J. S. Halekas (2012), A chain of magnetic flux ropes in the magnetotail of Mars, *Geophys. Res. Lett.*, *39*, L03104, doi:10.1029/2011GL050444.

Edberg, N. J. T., et al. (2009a), Rosetta and Mars Express observations of the influence of high solar wind pressure on the Martian plasma environment, *Ann. Geophys.*, *27*, 4533–4545, doi:10.5194/angeo-27-4533-2009.

Edberg, N. J. T., D. A. Brain, M. Lester, S. W. H. Cowley, R. Modolo, M. Fränz, and S. Barabash (2009b), Plasma boundary variability at Mars as observed by Mars Global Surveyor and Mars Express, *Ann. Geophys.*, *27*, 3537–3550, doi:10.5194/angeo-27-3537-2009.

Edberg, N. J. T., H. Nilsson, A. O. Williams, M. Lester, S. E. Milan, S. W. H. Cowley, M. Fränz, S. Barabash, and Y. Futaana (2010), Pumping out the atmosphere of Mars through solar wind pressure pulses, *Geophys. Res. Lett.*, *370*, L03107, doi:10.1029/2009GL041814.

Falkenberg, T. V., S. Vennerstrom, D. A. Brain, G. Delory, and A. Taktakishvili (2011a), Multipoint observations of coronal mass ejection and solar energetic particle events on Mars and Earth during November 2001, *J. Geophys. Res.*, *116*, A06104, doi:10.1029/2010JA016279.

Falkenberg, T. V., A. Taktakishvili, A. Pulkkinen, S. Vennerstrom, D. Odstrcil, D. Brain, G. Delory, and D. Mitchell (2011b), Evaluating predictions of ICME arrival at Earth and Mars, *Space Weather*, *9*, S00E12, doi:10.1029/2011SW000682.

Feng, X., S. Zhang, C. Xiang, L. Yang, C. Jiang, and S. T. Wu (2011), A hybrid solar wind model of the CESE + HLL method with a Yin-Yang overset grid and an AMR grid, *Astrophys. J.*, *734*, doi:10.1088/0004-637X/734/1/50.

Feng, X., L. Yang, C. Xiang, C. Jiang, X. Ma, S. T. Wu, D. Zhong, and Y. Zhou (2012), Validation of the 3D AMR SIP-CESE solar wind model for four Carrington rotations, *Sol. Phys.*, *279*, doi:10.1007/s11207-012-9969-9.

Feng, X., M. Zhang, and Y. Zhou (2014), A new three-dimensional solar wind model in spherical coordinates with a six-component grid, *Astrophys. J.*, *214*, doi:10.1088/0067-0049/214/1/6.

Ferguson, B. B., J. C. Cain, D. H. Crider, D. A. Brain, and E. M. Harnett (2005), External fields on the nightside of Mars at Mars Global Surveyor mapping altitudes, *Geophys. Res. Lett.*, *32*, L16105, doi:10.1029/2004GL021964.

Gressl, C., A. M. Veronig, M. Temmer, D. Odstrcil, J. A. Linker, Z. Mikić, and P. Riley (2014), Comparative study of MHD modeling of the background solar wind, *Sol. Phys.*, *289*, 1783–1801, doi:10.1007/s11207-013-0421-6.

Haider, S. A., K. K. Mahajan, and E. Kallio (2011), Mars ionosphere: A review of experimental results and modeling studies, *Rev. Geophys.*, *49*, RG4001, doi:10.1029/2011RG000357.

Hakamada, K., and S.-I. Akasofu (1982), Simulation of three-dimensional solar wind disturbances and resulting geomagnetic storms, *Space Sci. Rev.*, *31*, 3–70, doi:10.1007/BF00349000.

Halekas, J. S., J. P. Eastwood, D. A. Brain, T. D. Phan, M. Øieroset, and R. P. Lin (2009), In situ observations of reconnection Hall magnetic fields at Mars: Evidence for ion diffusion region encounters, *J. Geophys. Res.*, *114*, A11204, doi:10.1029/2009JA014544.

Halekas, J. S., E. R. Taylor, G. Dalton, G. Johnson, D. W. Curtis, J. P. McFadden, D. L. Mitchell, R. P. Lin, and B. M. Jakosky (2013), The Solar Wind Ion Analyzer for MAVEN, *Space Sci. Rev.*, doi:10.1007/s11214-013-0029-z.

Harten, A. (1983), High resolution schemes for hyperbolic conservation laws, *J. Comp. Phys.*, *49*, 357–393, doi:10.1016/0021-9991(83)90136-5.

Harvey, J. W., et al. (1996), The Global Oscillation Network Group (GONG) Project, *Science*, *272*, 1284–1286, doi:10.1126/science.272.5266.1284.

Hayashi, K. (2012), An MHD simulation model of time-dependent co-rotating solar wind, *J. Geophys. Res.*, *117*, A08105, doi:10.1029/2011JA017490.

Intriligator, D. S., W. Sun, M. Dryer, J. Intriligator, C. Deehr, T. Detman, and W. R. Webber (2015a), Did the July 2012 solar events cause a "tsunami" throughout the heliosphere, heliosheath, and into the interstellar medium?, *J. Geophys. Res. Space Physics*, *120*, 8267–8280, doi:10.1002/2015JA021406.

Intriligator, D. S., W. Sun, W. D. Miller, M. Dryer, C. Deehr, W. R. Webber, J. M. Intriligator, and T. M. Detman (2015b), Modelling the March 2012 solar events and their impacts at Voyager 1 in the vicinity of the heliopause, *J. Phys. Conf. Ser.*, *577*, doi:10.1088/1742-6596/577/1/012013.

Jakosky, B. M., et al. (2015a), MAVEN observations of the response of Mars to an interplanetary coronal mass ejection from the Sun, *Science*, *350*, doi:10.1126/science.aad0210.

Jakosky, B. M., et al. (2015b), The Mars Atmosphere and Volatile Evolution (MAVEN) mission, *Space Sci. Rev.*, doi:10.1007/s11214-015-0139-x.

Jian, L. K., C. T. Russell, J. G. Luhmann, P. J. MacNeice, D. Odstrcil, P. Riley, J. A. Linker, R. M. Skoug, and J. T. Steinberg (2011), Comparison of observations at ACE and Ulysses with ENLIL model results: Stream interaction regions during Carrington rotations 2016–2018, *Sol. Phys.*, *273*, 179–203, doi:10.1007/s11207-011-9858-7.

Jian, L. K., P. J. MacNeice, A. Taktakishvili, D. Odstrcil, B. Jackson, H.-S. Yu, P. Riley, I. V. Sokolov, and R. M. Evans (2015), Validation for solar wind prediction at Earth: Comparison of coronal and heliospheric models installed at the CCMC, *Space Weather*, *13*, 316–338, doi:10.1002/2015SW001174.

Lee, C. O., J. G. Luhmann, D. Odstrcil, P. J. MacNeice, I. de Pater, P. Riley, and C. N. Arge (2009), The solar wind at 1 AU during the declining phase of solar cycle 23: Comparison of 3D numerical model results with observations, *Sol. Phys.*, *254*, 115–183, doi:10.1007/s11207-008-9280-y.

Lee, C. O., C. N. Arge, D. Odstrcil, G. Millward, V. Pizzo, J. M. Quinn, and C. J. Henney (2013), Ensemble modeling of CME propagation, *Sol. Phys.*, *285*, 349–368, doi:10.1007/s11207-012-9980-1.

Lee, C. O., N. Arge, D. Odstrcil, G. Millward, V. Pizzo, and N. Lugaz (2015), Ensemble modeling of successive halo CMEs: A case study, *Sol. Phys.*, *290*, 1207–1229, doi:10.1007/s11207-015-0667-2.

Liou, K., C.-C. Wu, M. Dryer, S.-T. Wu, N. Rich, S. Plunkett, L. Simpson, C. D. Fry, and K. Schenk (2014), Global simulation of extremely fast coronal mass ejection on 23 July 2012, *J. Atmos. Sol. Terr. Phys.*, *121*, doi:10.1016/j.jastp.2014.09.013.

Lundin, R., S. Barabash, A. Fedorov, M. Holmström, H. Nilsson, J.-A. Sauvaud, and M. Yamauchi (2008), Solar forcing and planetary ion escape from Mars, *Geophys. Res. Lett.*, *35*, L09203, doi:10.1029/2007GL032884.

Ma, Y., A. F. Nagy, I. V. Sokolov, and K. C. Hansen (2004), Three-dimensional, multispecies, high spatial resolution MHD studies of the solar wind interaction with Mars, *J. Geophys. Res.*, *109*, A07211, doi:10.1029/2003JA010367.

Mays, M. L., et al. (2015), Ensemble modeling of CMEs using the WSA-ENLIL + Cone model, *Sol. Phys*, doi:10.1007/s11207-015-0692-1.

McKenna-Lawlor, S. M. P., et al. (2008), Predicting interplanetary shock arrivals at Earth, Mars, and Venus: A real-time modeling experiment following the solar flares of 5–14 December 2006, *J. Geophys. Res.*, *113*, A06101, doi:10.1029/2007JA012577.

Millward, G., D. Biesecker, V. Pizzo, and C. A. de Koning (2013), An operational solftware tool for the analysis of coronagraph images: Determining CME parameters for input into the WSA-Enlil heliospheric model, *Space Weather*, *11*, 57–68, doi:10.1002/swe.20024.

Najib, D., A. F. Nagy, G. Tóth, and Y. Ma (2011), Three-dimensional, multifluid, high spatial resolution MHD model studies of the solar wind interaction with Mars, *J. Geophys. Res.*, *116*, A05204, doi:10.1029/2010JA016272.

Nilsson, H., E. Carlsson, D. A. Brain, M. Yamauchi, M. Holmström, S. Barabash, R. Lundin, and Y. Futaana (2010), Ion escape from Mars as a function of solar wind conditions: A statistical study, *Icarus*, *206*, 40–49, doi:10.1016/j.icarus.2009.03.006.

Odstrcil, D. (2003), Modeling 3-D solar wind structure, *Adv. Space Res.*, *32*, 497–506, doi:10.1016/S0273-1177(03)00332-6.

Opgenoorth, H. J., D. J. Andrews, M. Fränz, M. Lester, N. J. T. Edberg, D. Morgan, F. Duru, O. Witasse, and A. O. Williams (2013), Mars ionospheric response to solar wind variability, *J. Geophys. Res. Space Physics*, *118*, 6558–6587, doi:10.1002/jgra.50537.

Pizzo, V., G. Millward, A. Parsons, D. Biesecker, S. Hill, and D. Odstrcil (2011), Wang-Sheeley-Arge-ENLIL cone model transitions to operations, *Space Weather*, *9*, S033004, doi:10.1029/2011SW000663.

Schatten, K. H. (1971), Current sheet magnetic model for the solar corona, *Cosm. Electrodyn.*, *2*, 232–245.

Schatten, K. H., J. M. Wilcox, and N. F. Ness (1969), A model of interplanetary and coronal magnetic fields, *Sol. Phys.*, *6*, 442–455, doi:10.1007/BF00146478.

Tóth, G., and D. Odstrcil (1996), Comparison of some flux corrected transport and total variation diminishing numerical schemes for hydrodynamic and magnetohydrodynamic problems, *J. Comput. Phys.*, *128*, 82–100, doi:10.1006/jcph.1996.0197.

Tóth, G., et al. (2005), Space Weather Modeling Framework: A new tool for the space science community, *J. Geophys. Res.*, *110*, A12226, doi:10.1029/2005JA011126.

Tóth, G., et al. (2012), Adaptive numerical algorithms in space weather modeling, *J. Comp. Phys.*, *231*, 870, doi:10.1016/j.jcp.2011.02.006.

Vennerstrom, N. Olsen, M. Purucker, M. H. A., and J. C. Cain (2003), The magnetic field in the pile-up region at Mars, and its variation with the solar wind, *Geophys. Res. Lett.*, *30*, 1369, doi:10.1029/2003GL016883.

Wang, Y.-M., and N. R. Sheeley Jr. (1992), On potential field models of the solar corona, *Astrophys. J.*, *392*, 310–319.

Wei, Y., et al. (2012), Enhanced atmospheric oxygen outflow on Earth and Mars driven by a corotating interaction region, *J. Geophys. Res.*, *117*, A03208, doi:10.1029/2011JA017340.

Wu, C.-C., M. Dryer, S. T. Wu, B. E. Wood, C. D. Fry, K. Liou, and S. Plunkett (2011), Global three-dimensional simulation of the interplanetary evolution of the observed geoeffective coronal mass ejection during the epoch 1–4 August 2010, *J. Geophys. Res.*, *116*, A12103, doi:10.1029/2011JA016947.

Wu, C.-C., K. Liou, A. Vourlidas, S. Plunkett, M. Dryer, S. T. Wu, and R. A. Mewaldt (2016a), Global magnetohydrodynamic simulation of the 15 March 2013 coronal mass ejection event—Interpretation of the 30–80 MeV proton flux, *J. Geophys. Res. Space Physics*, *121*, 56–76, doi:10.1002/2015JA021051.

Wu, C.-C., K. Liou, A. Vourlidas, S. Plunkett, M. Dryer, S. T. Wu, D. Socker, B. E. Wood, L. Hutting, and R. A. Howard (2016b), Numerical simulation of multiple CME-driven shocks in the month of 2011 September, *J. Geophys. Res. Space Physics*, *121*, 1839–1856, doi:10.1002/2015JA021843.

Wu, S. T., Y. Zhou, C. Jiang, X. Feng, C.-C. Wu, and Q. Hu (2016), A data-constrained three-dimensional magnetohydrodynamic simulation model for a coronal mass ejection initiation, *J. Geophys. Res. Space Physics*, *121*, 1009–1023, doi:10.1002/2015JA021615.

Xie, H., L. Ofman, and G. Lawrence (2004), Cone model for halo CMEs: Applications to space weather forecasting, *J. Geophys. Res.*, *109*, A03109, doi:10.1029/2003JA010226.

Xie, H., D. Odstrcil, L. Mays, O. C. S. Cyr, N. Gopalswamy, and H. Cremades (2012), Understanding shock dynamics in the inner heliosphere with modeling and Type II radio data: The 2010-04-03 event, *J. Geophys. Res.*, *117*, A04105, doi:10.1029/2011JA017304.

Yang, L. P., X. S. Feng, C. Q. Xiang, Y. Liu, X. Zhao, and S. T. Wu (2012), Time-dependent MHD modeling of the global solar corona for year 2007: Driven by daily-updated magnetic field synoptic data, *J. Geophys. Res.*, *117*, A08110, doi:10.1029/2011JA017494.

Yang, L., X. Feng, C. Xiang, S. Zhang, and S. T. Wu (2011), Simulation of the unusual solar minimum with 3D SIP-CESE MHD model by comparison with multi-satellite observations, *Sol. Phys.*, *271*, doi:10.1007/s11207-011-9785-7.

Zhao, X. P., S. P. Plunkett, and W. Liu (2002), Determination of geometrical and kinematical properties of halo coronal mass ejections using the cone model, *J. Geophys. Res.*, *107*(A8), 1223, doi:10.1029/2001JA009143.